

Process Mechanics of Low Plasticity Burnishing of Nitinol Alloy

C.H. Fu, Y.B. Guo, J. McKinney, and X.T. Wei

(Submitted March 16, 2012; in revised form May 31, 2012)

Nitinol alloys have received considerable attention in biomedical and aerospace applications. Surface integrity of Nitinol devices by various manufacturing processes is crucial for their functionality. Low plasticity burnishing (LPB) is very promising to modify surface integrity due to its unique capability to adjust material properties down to the deep subsurface on the order of a few millimeters. Burnishing mechanics is essential to understand its effect on surface properties. The depth and width of burnished surface materials are characterized. A three-dimensional finite element simulation has been developed to incorporate the superelastic mechanical behavior of Nitinol. The simulation predictions are validated with the experimental results. The contact stresses, residual stresses, and strain profiles are investigated to better understand burnishing mechanics.

Keywords burnishing, finite element analysis, medical device, nitinol, process mechanics

1. Introduction

1.1 Nitinol Alloy

Nitinol is a nickel-titanium alloy of near-equiatomic composition with superelastic (SE) mechanical properties as well as shape memory properties. Slight variations in the binary alloy composition change the mechanical properties significantly; moreover, heat treatment history and finishing of the material play a vital role in the mechanical properties as well. Typically, superelasticity occurs at elevated temperatures that approach the melting point of the material. Nitinol is composed of nickel and titanium and the accompanying characteristics of both metals distinguish the overall properties of a superalloy. Nitinol has SE features well below the melting point. As a result, these material properties are advantageous to various biomedical and aerospace applications. Nitinol was first discovered in the early 1960s, and some of the first experimental study was conducted by the Naval Ordnance Laboratory. Many of the early applications of Nitinol focused on the shape memory effect, whereas in the recent years, a lot of attention has been aimed toward the superelasticity of Nitinol with particular emphasis in biomedical applications. The physiological conditions of the in

vivo environment within the human body are isothermal where the temperature of the body turns out to be ideal for the SE properties of binary Nitinol (Ref 1). The nonlinear effect of the superelasticity of Nitinol is based on a mechanical event where a diffusionless fully reversible phase transformation evolves. The superelasticity effect of Nitinol originates in an austenitic parent phase where the continued application of stress results in a martensitic phase evolution, and this stress-induced phase transition is commonly referred to as stress-induced martensite (SIM). Nitinol is an ordered intermetallic that has an extremely narrow composition range below 630 °C the eutectoid in the phase diagram (Ref 2, 3).

1.2 Surface Integrity

Surface integrity of Nitinol is important for the resistance to corrosion and wear which are primary failure mechanisms in Nitinol devices and components. Surface integrity of a Nitinol device has been shown to correlate the biocompatibility of biomedical Nitinol devices and components (Ref 4) where the poor surface finish of biomedical Nitinol devices and components has been shown to produce poor resistance to corrosion (Ref 5). The contribution to high wear resistance of Nitinol is due to several factors, such as pseudoelasticity, strain hardening, as well as hardness (Ref 4, 6). Hence, it shows that a surface modification process is able to enhance these features of a Nitinol implantation device for improving the ability to mitigate corrosion and wear.

1.3 Low Plasticity Burnishing (LPB)

Owing to the elegant nature of (50.8 at.% Ni-49.2 at.% Ti) SE Nitinol, recent attention has been focused on biomedical applications. It is critical that the material has superior resistance to corrosion with excellent fatigue life while meeting and exceeding Food and Drug Administration (FDA) guidelines. According to the 2010 guideline established by FDA, it is recommended that vascular stents undergo bench-top pulsatile fatigue testing replicating pressure cycles at accelerated frequencies relative to human conditions. Hence, this particular

This article is an invited paper selected from presentations at the International Conference on Shape Memory and Superelastic Technologies 2011, held November 6-9, 2011, in Hong Kong, China, and has been expanded from the original presentation.

C.H. Fu, Y.B. Guo, and J. McKinney, Department of Mechanical Engineering, The University of Alabama, Tuscaloosa, AL 35487; and X.T. Wei, School of Mechanical Engineering, Shandong University of Technology, Zibo, China. Contact e-mails: fuchenhao 2009@gmail.com and yguo@eng.ua.edu.

Nomenclature	
E^*	Effective Modulus
E_1	Elastic modulus of the tool
E_2	Elastic modulus of the workpiece
ν_1	Poisson's ratio of the tool
ν_2	Poisson's ratio of the workpiece
R	Effective curvature
R_1	Curvature of tool
R_2	Curvature of the workpiece
F	Burnishing force
P	Load input
r	Radius of the tool
a	Contact radius
p_0	Maximum contact pressure
δ	Approach of distant points
τ_1	Maximum shear stress
σ_r	Maximum tensile stress
$\sigma_{1,2,3}$	Principal stresses
E_a	Austenite elasticity
ν_a	Austenite Poisson's ratio
E_m	Martensite elasticity
ν_m	Martensite Poisson's ratio
ε^L	Transformation strain
$(\frac{\delta\sigma}{\delta T})^L$	$(\frac{\delta\sigma}{\delta T})$ loading
σ_L^S	Start of transformation loading
σ_L^E	End of transformation loading
T_0	Reference temperature
$(\frac{\delta\sigma}{\delta T})^U$	$(\frac{\delta\sigma}{\delta T})$ unloading
σ_u^S	Start of transformation unloading
σ_u^E	End of transformation unloading
σ_{CL}^E	Start of transformation stress during loading in compression, as a positive value
ε_V^L	Volumetric transformation strain
N_p	Number of stress-strain pairs to define yield curve
$\sigma_1^p, \varepsilon_1, \dots, \sigma_{11}^p, \varepsilon_{11}$	Stress-strain points in the yield curve
S22	Normal stress in width direction
S33	Normal stress in depth direction
PE33	Plastic strain in depth direction
z	Distance underneath the surface

guideline indicates that a fatigue life requirement of 10 years equivalent to human in vivo physiological conditions substantiates sufficient proof of safety for most patients (Ref 7, 8). Low plasticity burnishing (LPB) is a surface-finishing technique adopted to tailor surface integrity for specific applications. LPB is a low plasticity process that enhances surface integrity features such as roughness and hardness while providing longer fatigue life (Ref 9, 10). LPB is known for producing high compressive residual stresses in the deeper subsurface, which has been attributed to longer high-cycle fatigue life. LPB provides a deep stable layer of compressive residual stresses in nickel, titanium, steels, and aluminum alloys that can exceed 1 mm in depth, which typically exceed the depth of typical corrosion pits (Ref 10, 11). LPB is unique in the respect that it employs low plastic cold work, usually less than 3-5% (Ref 12, 13), where typical surface-modification processes such as shot peening often produce cold work greater than 80% (Ref 2). A conventional CNC milling machine can be used to implement the process with respect to the desired workspace. Hence, it is

thereby hypothesized that LPB would be an enabling surface-modification process to improve surface integrity of SE Nitinol biomedical devices.

1.4 Research Objectives

LPB has a great potential to surface treatment of Nitinol alloys for improving fatigue life. However, very little study has been done to understand the basic process mechanics of LPB of Nitinol alloys. Furthermore, the previous studies on burnishing steel alloys are mostly limited two-dimensional (2D) simulations (Ref 14, 15). SE508 Nitinol has a unique stress-strain response including phase transformation upon mechanical loading. Therefore, this research aims to provide a deeper understanding to process mechanics of burnishing SE508 Nitinol. The objectives of the study are to (1) develop a 3D finite element simulation of ball burnishing to provide a basic understanding of process mechanism; (2) predict the contact pressure to induce plastic deformation under the applied load; and (3) gain insight into the stress/strain development in ball burnishing.

2. LPB Experiment

2.1 Experimental Setup

The LPB was performed using a Cincinnati Arrow 2 CNC machine. The process is implemented with the use of a high modulus freely rotating spherical ball that is rolled over the workpiece surface under applied pressures (Ref 16). A schematic of LPB process is seen in Fig. 1.

A fixture design was necessary to conduct LPB experiments. The fixture design allows the use of a load cell such that the applied load could be measured to verify LPB process parameters. Figure 2 illustrates the fixture where a cavity on the top face of the fixture, along with a peripheral fitting, was machined to securely hold the workpiece such that steady-state operating conditions can be ensured. The top plate of the fixture rests on four posts where a load cell securely rests below, capturing the load data during operation. The Ecoroll LPB tool

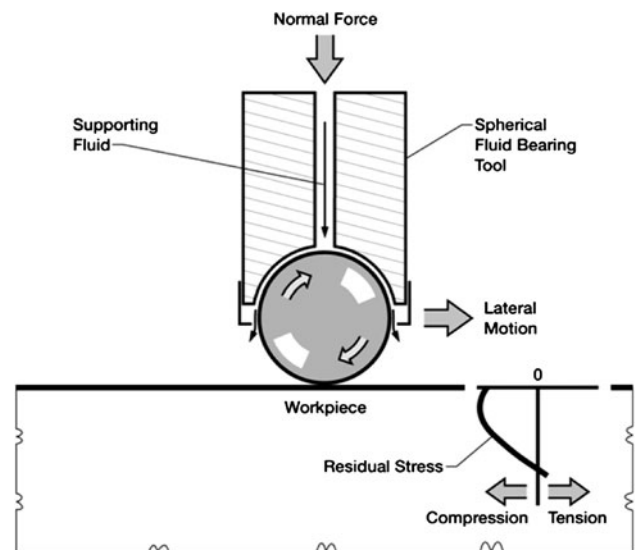


Fig. 1 Schematic of LPB

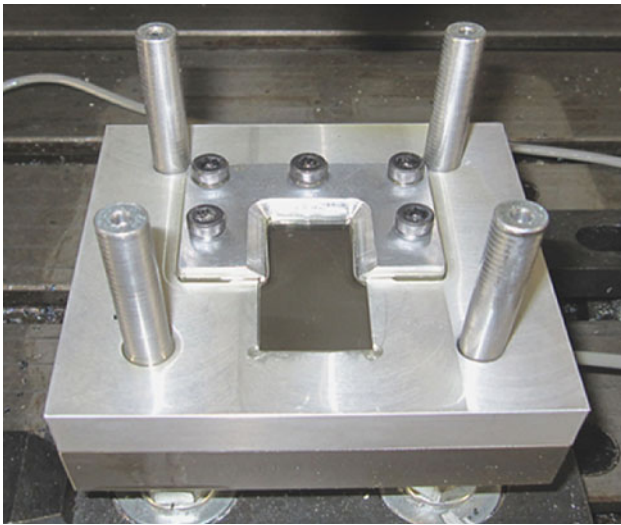


Fig. 2 LPB fixture design

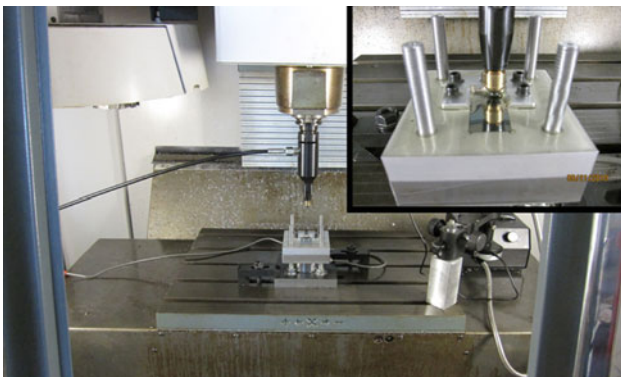


Fig. 3 LPB experimental setup

with a 12.7-mm ball diameter was used. The LPB tool was moved at a constant speed of 1000 mm/min in this experiment. The high pressures by the LPB tool are controlled by hydraulic fluid that tends to spill on the workpiece and surrounding areas. The hydraulic fluid is machine friendly and acts as a coolant. The burnishing experimental setup is shown in Fig. 3.

2.2 SE508 Work Material

The work material used is SE Nitinol SE508 (55.8 wt.% Ni-44.2 wt.% Ti) in thin sheet form. The particular compositions of binary nickel-titanium are commonly used in

Table 1 Composition of the SE508 Nitinol

Nickel (nominal)	55.8 wt.%
Titanium	Balance
Oxygen (max)	0.05 wt.%
Carbon (max)	0.02 wt.%

Table 2 Material properties of the LPB ball

E^* , MPa	E_1 , MPa	E_2 , MPa	ν_1	ν_2	R , mm	R_1 , mm	R_2 , mm	r , mm
37162	315000	37998	0.26	0.3	6.35	6.35	∞	6.35

biomedical applications as the mechanical properties are similar to those of biological tissues (Ref 17). The average grain size of the as-received austenitic parent phase Nitinol sheet samples were on the order of $\sim 40 \mu\text{m}$. Cold working is capable of transforming the parent austenite phase into a martensite phase by localized stress distributions (SIM) (Ref 18). The as-received Nitinol sheets are 1.5 mm in thickness and were cut to size by electrical discharge machining, and mechanically polished to a mirror finish to allow for precise measurement of burnished surface profiles (Ref 19). Similarly, a smooth surface contact to the burnishing ball allows for better accuracy in characterizing the experimental results. Table 1 illustrates the composition of SE508 Nitinol.

3. LPB Process Analysis

3.1 Burnishing Pressure/Force

The objective is to induce small amounts of uniform plasticity where the tool is in contact with the surface of the workpiece. The quasi-static mechanical properties of SE508 Nitinol may serve as a guideline to determine the critical region of desired plasticity. Hertz theory of elastic contact may be employed within the limits of small deformation (Ref 20, 21) to characterize the applied LPB loads for SE508 Nitinol. When considering the force input for LPB process, it is important to quantify several parameters such as the tool radius, the effective curvature, and stiffness of the tool with respect to the workpiece. These input variables may be quantified by the following equations of Hertz elastic contact.

$$E^* \equiv \left(\frac{1 - \nu_1^2}{E_1} + \frac{1 - \nu_2^2}{E_2} \right)^{-1} \quad (\text{Eq 1})$$

$$\frac{1}{R} \equiv \left(\frac{1}{R_1} + \frac{1}{R_2} \right) \quad (\text{Eq 2})$$

$$F = P\pi r^2 \quad (\text{Eq 3})$$

The material properties of the Ecoroll LPB ball and the workpiece are listed in Table 2. The effective modulus considers the tool and the workpiece; however, the workpiece has two regions of elasticity where the austenitic and martensitic elastic regions were averaged as the overall modulus of elasticity for the workpiece. Since the workpiece is a thin plate of infinite curvature, the value of R_2 is null.

3.2 Peak Pressure Versus Stress-Strain Curve

The peak Hertz pressure p_0 is consistent with the true stress at the corresponding strains in the quasi-static stress-strain curve of SE508 Nitinol. The experimental plan of this investigation is based on Hertz contact theory of elastic bodies, and such corresponding values may be observed in Table 3. The theoretical pressure values are plotted with the measured

Table 3 LPB experiment plan

Sample #	Pressure, MPa	F, N	p_o , MPa	a , mm	δ , μm	τ_{max} , MPa	σ at $r = a$, MPa
1	0.15	19	500	0.13	3	155	67
2	0.61	77	800	0.21	7	248	107
3	1.19	151	1000	0.27	11	310	133
4	4.02	509	1500	0.40	26	465	200
5	9.53	1207	2000	0.54	45	620	267
6	13.57	1719	2250	0.60	57	698	300
7	15	1900	2327	0.62	61	721	310
8	20	2534	2561	0.69	74	794	341

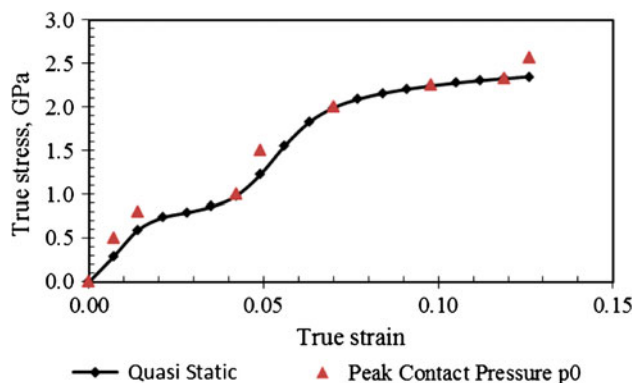


Fig. 4 Quasi-static mechanical properties compared with Hertz peak pressure

Table 4 Pressure vs. burnishing depth/width

Pressure, MPa	Depth, μm	Width, μm	Contact radius, μm
0.15	134.2
0.61	214.7
1.19	268.4
4.02	0.17	1648.2	402.7
9.53	0.34	1814.8	536.8
13.57	1.33	1879.7	603.9
15	1.14	1666.7	624.5
20	4.18	2018.5	687.3

quasi-static stress-strain mechanical properties in Fig. 4. In the theoretical curve, the pressure values were determined by Hertzian theory, and the corresponding strain values were selected according to the experimental stress-strain response of the material. This plot suggests that values of Hertz peak pressures correspond to true stress and strain values and may serve as a valuable tool in determining the LPB input pressures. Based on Hertzian elastic contact, the contact radius of the spherical indenter is a function of the input load as well as the effective stiffness and curvatures of the two elastic materials in contact. The maximum contact pressure derives from load input with respect to the burnishing ball. Furthermore, the burnishing depth is a function of load input, ball geometry, and an overall effective stiffness. These values may be obtained from the following equations:

$$a = \left(\frac{3PR}{4E^*} \right)^{1/3} \quad (\text{Eq 4})$$

$$p_o = \left(\frac{3P}{2\pi a^2} \right) \quad (\text{Eq 5})$$

$$\delta = \left(\frac{9}{16} \frac{P^2}{RE^{*2}} \right)^{1/3} \quad (\text{Eq 6})$$

3.3 Track Depth/Width

During spherical indentation on the surface of a flat contact area, the effects of sink-in and pile-up occur where the load is applied. When the indented material is deformed elastically, the effect of sinking-in occurs. However, when the indented material exceeds the yield stress, the increase in plastic deformation of the indented material has a decrease in sinking-in and an increase in pile-up. The presence of these particular characteristics causes inaccuracies in determining the projected area of contact (Ref 22). It is important to establish a high degree of accuracy when evaluating the true contact area geometry, yet the contact area from indentation load-depth data is not necessarily a straightforward process, as there is a dependence on the amount of pile-up or sink-in of material around the edge of the indentation (Ref 20, 23). Moreover, the effect of pile-up is influenced by loading pressure and the strain hardening mechanical properties of the work material. A general trend can be noted, whereas the increase of pressure increases dislocation density with the microstructure of the material and is the dominant factor affecting fatigue life. However, there are a combined series of factors that influence the hardness and surface roughness of the material and not a single stand-alone factor (Ref 11). In biomedical applications, the effect of superelasticity is the attractive property of Nitinol and it is vital to preserve the SE features. The amount of cold work induced by LPB is of low magnitude, and yet the fatigue life can substantially be increased as well as corrosion performance standards. The highest level of cold work induced in this study was 0.2%. Dektak II surface profilometer was used to measure the depth and width of burnished profiles. A governing factor of the LPB process is the size of the tool tip and the applied pressure, whereby an acceptable feed may be established. Table 4 illustrates the LPB pressures with respect to contact width, depth, and contact radius. It was found that the width of the indentation tracks changed very little with the increase of pressure although the track width was substantially larger

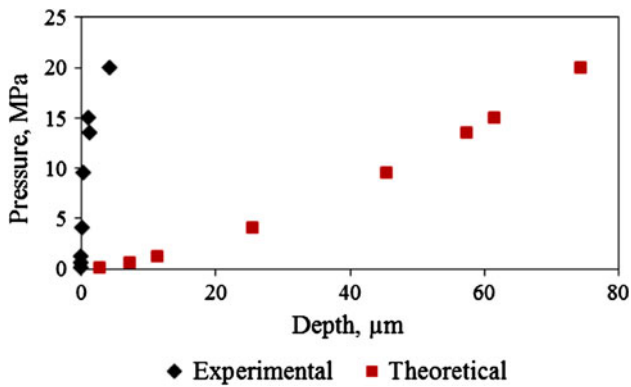


Fig. 5 Burnishing pressure vs. theoretical and experimental depth

than the penetration depth, which was expected. The contact radius pertains to the Hertzian contact model of an elastic solid. Table 4 shows that the first three burnishing pressures caused only elastic indentation.

3.4 Maximum Shear Stress and Location in Subsurface

When two elastic solid bodies come into contact, the onset of plasticity is dependent on the hardness of the two bodies and loading conditions. For this particular contact problem, the initiation of plastic yielding occurs beneath the surface while creating a stress field. Expressions for the subsurface shear stresses may be observed in Eq 7 for $\nu = 0.3$ (Ref 20). A linear relationship exists with the Hertzian theoretical values of shear stress and subsurface location. Moreover, a general rule of thumb is that the locations of subsurface maximum shear stresses are about half the distance of the contact radius. This particular characteristic is ideal for generating deep subsurface compressive residual stresses by the use of LPB with a spherical tool tip. The magnitude of the stress field increases as indentation depth or force increases. Once the stress field reaches an equivalent point within the specimen, the material will start to transform to martensite with an increasing hardness (Ref 21, 24). According to Hertz theory of contact mechanics, it can be observed in Eq 7 that the maximum shear stress is 31% of the applied maximum contact pressure applied at the center of contact. The Hertzian contact solutions hold true in a purely elastic state, and a generalized Von Mises Stress criterion is commonly used as a yielding envelope. Based on the average of the principal stresses with the Von Mises criterion, it can be assumed that plastic flow occurs when the distortional strain energy reaches a critical value, and the result of the initiated yielding may be observed in Eq 8.

A factor of consideration for the Hertzian contact mechanics is the sensitivity of Poisson's ratio with respect to the contact angle. The load case of a spherical surface in contact with an infinitely flat surface also bears the consideration of the contact angles and the effect of the surface and subsurface stresses (Ref 25, 26). Similarly, the maximum tensile stress for this load case may be ascertained by Eq 9, where the maximum tensile stress resides at the surface of the work material just outside the contact patch. The radial stress is therefore tensile outside the loaded area. It reaches a maximum value at the edge of the circle at $r = a$. This is the maximum tensile stress occurring anywhere (Ref 20). We can observe that the Poisson effect is a parameter

involved in the generated tensile stress field, whereby a stress deviator has the propensity to exist. It would also be desirable to the intended application for smooth surface to surface contact where many studies indicate the difficulty in the assumptions of classical Hertzian contact mechanics with relation to surface and subsurface stress fields.

Hertz theory of contact mechanics between two elastic bodies imposes the assumption that the contact surfaces are topographically smooth, whereby perfect contact takes place. In reality, all surfaces are rough to some extent where the true contact takes place at the crest of the surface asperities (Ref 19). Therefore, it implies that smoother surfaces allow for a higher degree of accuracy in determining surface and subsurface stress fields. This becomes an important factor in regard to subsurface residual stresses and the LPB process.

$$\tau_1 = 0.31p_0, \text{ at } r = 0, z = 0.48a \quad (\text{Eq 7})$$

$$(\sigma_1 - \sigma_2)^2 + (\sigma_2 - \sigma_3)^2 + (\sigma_3 - \sigma_1)^2 = 2\sigma_y^2 \quad (\text{Eq 8})$$

$$\sigma_r = \frac{1}{3}(1 - 2\nu_2)p_0, \text{ at } r = a, z = 0 \quad (\text{Eq 9})$$

4. Experimental Results

4.1 Characterization of Burnishing Tracks

On the premise that small deformations are imposed upon SE508 Nitinol in this experiment, Hertz theory of contact can be used for a basis model. There are challenges involved with predicting an accurate baseline model when the elastic range of the material is far beyond conventional. The aforementioned experimental plan constitutes the basis of the burnished pressures based on the Hertzian maximum contact pressure and experimentally determined compressive quasi-static stress-strain values. The springback due to superelasticity may be observed in Fig. 5.

Hence, it is necessary to experimentally determine process parameters for LPB. It was determined that the first three applied loads were purely elastic, and the critical threshold to induce plastic deformation was established at approximately 4 MPa with respect to a tool tip diameter of 12.7 mm. The depth of penetration in Hertz theory of contact mechanics resides in the elastic region, and therefore, does not indicate permanent indentation. However, it is interesting to note the difference of the indentation depth induced by plasticity in comparison with Hertz theory of elastic contact. While Hertz contact mechanics is not a gage of the plastic depth of penetration, we can ascertain that there is a large region of elastic springback of this material. We can also use this methodology to predict elasto-plasticity and the evolution of fully-plastic behavior upon the critical threshold of the burnishing pressure to induce plasticity. Past studies indicate that relatively high values of pressure and speed are the dominating factors where tool speed is a dominating factor in post-processing efficiency. The speed, or dwell time, of the tool has an effect of the evolution of plasticity, yet the tool speed was kept at a relatively high value in comparison with literature values obtained, in an effort to achieve post-processing efficiency and longer fatigue life (Ref 18). An investigation by Seemikeri et al. (Ref 18) reflected that the dominating

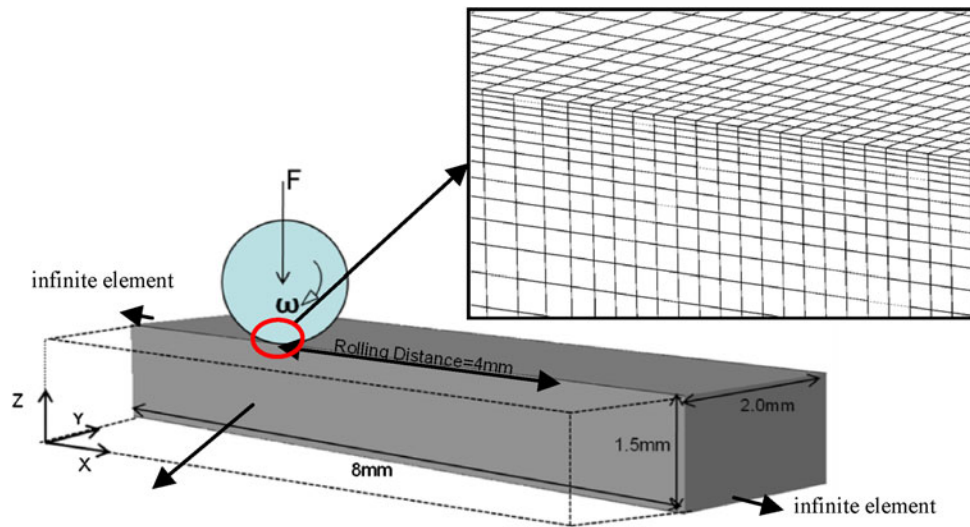


Fig. 6 3D FEA of burnishing (not to scale)

parameter was the applied pressure for increasing fatigue life, whereby there was no single factor that could solely have an effect on surface roughness, but a combination of parameters. We can expect that there will be greater hardness and pile-up when the spherical tool tip has greater contact area (Ref 23, 27, 28). As one would expect, the track profiles vary in depth with respect to pressure inputs. However, Table 4 shows that there is very little variance in width of each profile tracks. There was undetectable depth penetration with the first three pressure inputs, although the remaining pressure inputs reflected depth penetrations ranging from 0.2 to 4.0 μm with a percent cold work ranging from 0.01 to 0.2%, respectively. The cold work involved in LPB is rather small, and therefore the SE properties of SE508 Nitinol are not compromised.

5. Finite Element Analysis Procedure

5.1 Mesh

A 3D finite element model was developed to simulate LPB of SE508 Nitinol using ABAQUS/Explicit (Ref 29). The advantage of the explicit solver is that it is considered to be inexpensive both in time and space as a large number of equations are not required to be solved simultaneously. However, its drawback is that a convergence is not guaranteed.

The finite element mesh for burnishing is presented in Fig. 6. The workpiece is 1.5 mm in depth which is consistent with actual experimental sample. The width and length of the sample are 2 and 8 mm, respectively. This simulation consists of two steps. The first step is to roll the ball on workpiece with an applied load, and the second step is to remove applied load and lift up the ball. The ball is assumed to be rigid to reduce the computational time since the elastic modulus of the ball is much higher than the workpiece. The ball has an applied load

in the center, and it is assigned with a rotational speed ω . The rolling distance is 4 mm along positive X direction. The starting point of rolling is 2 mm away from the left edge. The model is designed to be symmetric about X-Z plane to simplify the simulation process and decrease the computational time. The workpiece contains both 8-node 3D finite element with temperature degree of freedom (C3D8RT) and 8-node semi-infinite element (CIN3D8). Semi-infinite elements were used along the left and right surfaces to ensure a non-reflective boundary. This model has 472,628 elements and 503,745 nodes. At the ball/workpiece contact zone, a fine mesh is used. In the far field where there is no contact, a coarse mesh is used. The fine-mesh region consists of 10- μm long, 10- μm wide, and 2- μm deep elements. These fine elements were used to provide a suitable spatial resolution with respect to output variables. The friction coefficient is assumed to be 0.05 to simulate the highly lubricated interface between the ball and workpiece.

5.2 Loading Condition

Two loads were used in the burnishing simulations, and the resulting burnished tracks were measured. These two loads are chosen to produce a plastic deformation on the workpiece. The specific loading condition is listed in Table 5.

5.3 Modeling of SE-Plastic Behavior of SE508

In order to model the SE-plastic behavior of SE508 Nitinol, a built-in user material subroutine was used in ABAQUS (Ref 29), the material inputs are obtained by a curve fitting the experimental data in uniaxial compression to the theoretical stress-strain curve (Fig. 7), under the assumption that tension and compression curve are symmetric with each other. The material constants are listed in Table 6.

6. Simulation Results

6.1 Dent Profiles Versus Experimental Data

The comparison between the predicted track profile and experimental track profile under load 1 is shown in Fig. 8.

Table 5 LPB loading in FEA simulations

Load 1, N	Load 2, N
2540.79	1716.75

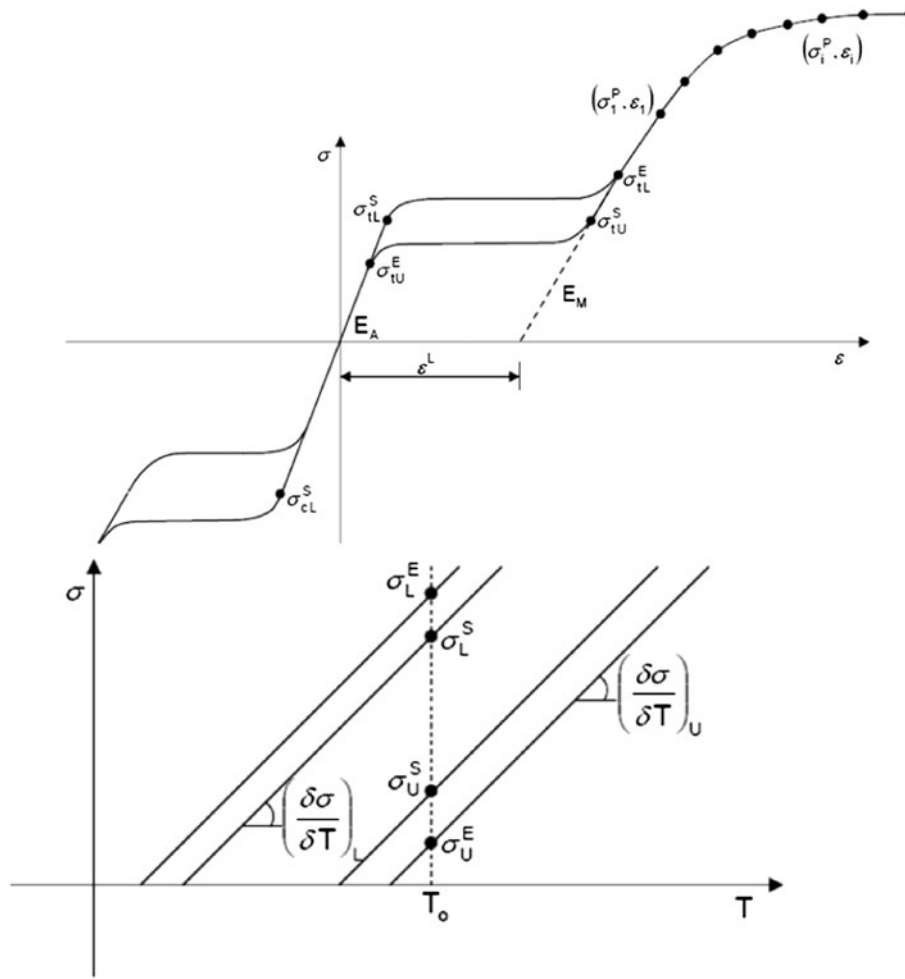


Fig. 7 SE-plastic behavior based on the uniaxial behavior (Ref 29)

Table 6 Material constants of SE508 Nitinol

Material parameter	Material constant	Material parameter	Material constant
E_a , Pa	4.23e+10	σ_3^p , Pa	1.990e+9
V_a	0.3	ϵ_3	0.070
E_m , Pa	4.29e+10	σ_4^p , Pa	2.088e+9
V_m	0.3	ϵ_4	0.077
ϵ^L	0.02	σ_5^p , Pa	2.155e+9
$(\frac{\delta\sigma}{\delta T})_L$	0	ϵ_5	0.084
σ_L^S , Pa	6.00e+8	σ_6^p , Pa	2.203e+9
σ_L^E , Pa	1.20e+9	ϵ_6	0.091
T_0 , °C	22	σ_7^p , Pa	2.424e+9
$(\frac{\delta\sigma}{\delta T})_U$	0	ϵ_7	0.098
σ_U^S , Pa	5.00e+8	σ_8^p , Pa	2.275e+9
σ_U^E , Pa	2.00e+8	ϵ_8	0.105
σ_{cL}^E , Pa	6.00e+8	σ_9^p , Pa	2.302e+9
ϵ_V^L	0.02	ϵ_9	0.112
N_p	11	σ_{10}^p , Pa	2.325e+9
σ_1^p , Pa	1.556e+9	ϵ_{10}	0.119
ϵ_1	0.056	σ_{11}^p , Pa	2.343e+9
σ_2^p , Pa	1.825e+9	ϵ_{11}	0.126
ϵ_2	0.063		

Three paths toward width direction were taken on rolling pass. Track profile of each path was plotted. In addition, an average track profile was also plotted. The simulated track width is approximately 2 mm, and the depth is 2.5 μm . In general, there

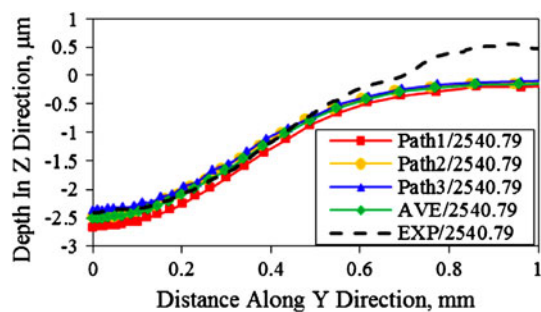


Fig. 8 Experimental and simulated track profiles

is a good agreement between simulation result and experimental result with regard to deformation and track shape. However, as is shown in Fig. 8, there is no “pile-up” effect observed in simulation while there is a “pile-up” with a height of 0.5 μm in experiment. This discrepancy might be due to the assumption of pure rolling in the simulation. Typically, a burnishing process is a combination of rolling and sliding contact. However, the measurement of percentage of each contact condition is next to impossible in experiment, and hence, is hard to simulate. In this study, with the consideration of the presence of lubricant and the freely rotating tool tip, the assumption of pure rolling contact is made.

6.2 Stress Profiles of Loaded Condition

Von Mises, S22, and S33 stresses along the depth direction at the two different loads are shown in Fig. 9(a), (b) and (c). In Fig. 9(a), the maximum Von Mises stress is 2.09 GPa occurring at 0.37 mm in subsurface for load 1. For load 2, a maximum

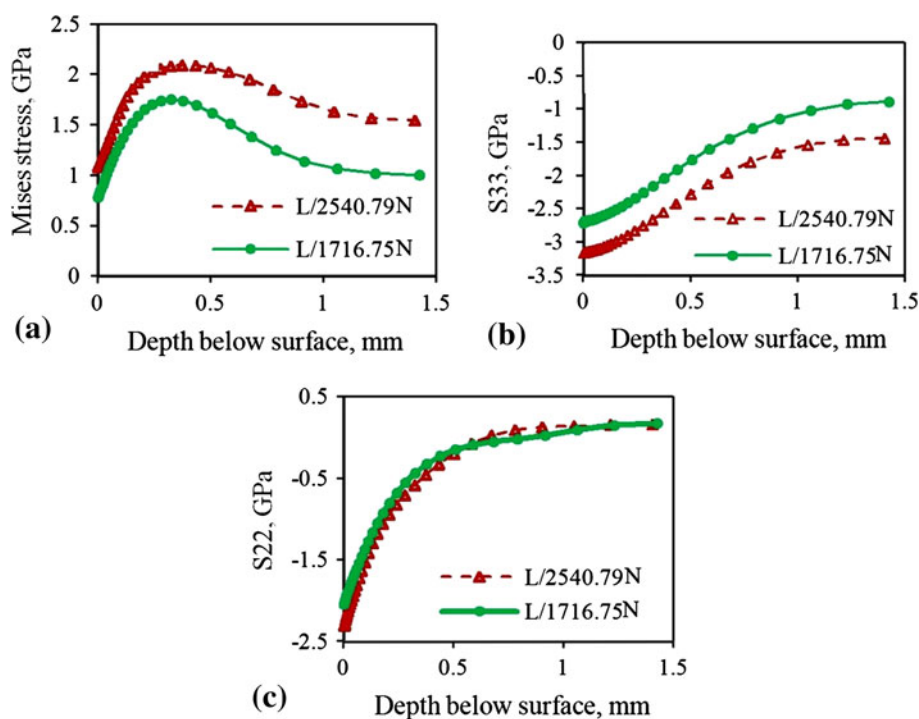


Fig. 9 Von Mises stress (a), S33 stress (b), and S22 stress (c) in subsurface

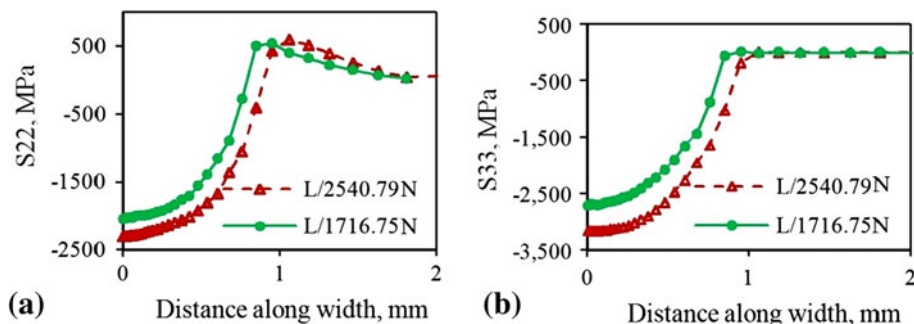


Fig. 10 S22 stress (a) and S33 stress (b) in width direction

stress of 1.75 GPa at a depth of 0.32 mm can be found. The magnitude of S33 stress will also increase with burnishing load. However, Fig. 9(c) shows that the increase in load does not affect the magnitude of S22.

As this is a 3D study, the stress profiles in width direction can also be studied. For both S22 and S33 (Fig. 10), there is a compression region up to 1 mm, and then S22 change from compression to tension, while S33 approaches to zero. With a greater applied load, the compression zone will be wider.

Figure 11(a) shows the subsurface shear stress contour (butterfly shape). This shear profile is symmetric with a change in sign at the center of contact. Figure 11(b-c) shows the cross-sectional shear stress contour inside the sample. This butterfly shape is a characteristic of rolling contact (Ref 9).

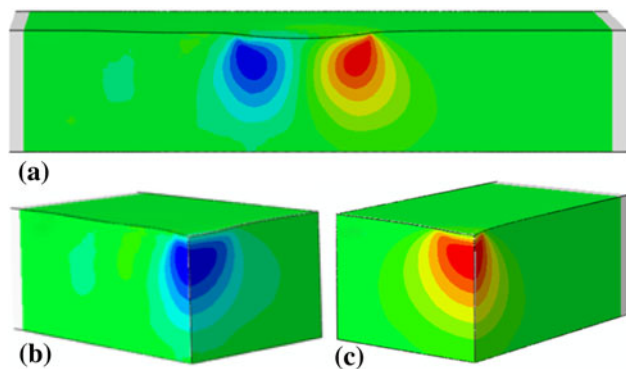


Fig. 11 3D contour of shear stress

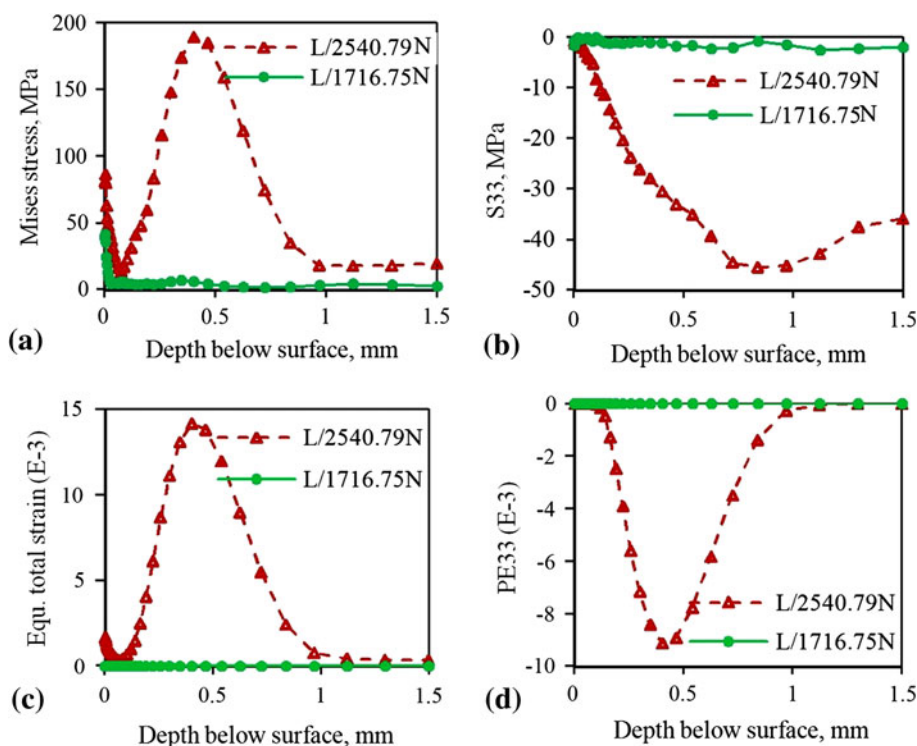


Fig. 12 Residual stress and strain profiles in subsurface

6.3 Residual Stress and Strain Profiles

The predicted residual Von Mises and S33 stress in depth direction are shown in Fig. 12(a) and (b). The S33 stress is tensile within the first 5 μ m, and then compressive residual stress is achieved. The maximum Von Mises stress occurs at 0.4 mm in subsurface, and axial compressive residual stress occurs at around 1.0 mm in subsurface for loading case 1. The magnitude of the S33 residual stress in subsurface is 45.4 MPa for loading case 1 and 2.5 MPa for loading case 2. As expected, the Von Mises stress penetrates deeper in subsurface for the larger load.

The equivalent total strain and plastic strain PE33 in subsurface are shown in Fig. 12(c) and (d). It can be observed that a subsurface “plastic zone” from 0.1 to 1 mm below the surface for loading case 1. It can be inferred that with an increasing applied load, both the magnitude of residual strain and the width of the plastic zone will increase.

When comparing the depth of maximum S33 and PE33, it is seen that the compressive residual stress depth is about two times deeper than the plastic residual strain in Fig. 13. This indicates that compressive residual stress in the deep subsurface is achieved with only a small amount of plastic deformation, which is a unique characteristic of LPB process.

6.4 Convergence Analysis

In order to verify the stability of the simulation results, a convergence analysis was performed by changing element size. The element number changes from 90 to 472,628. The deformation at the rolling ending point was taken as Y-axis in Fig. 14. It is illustrated that as the number of elements

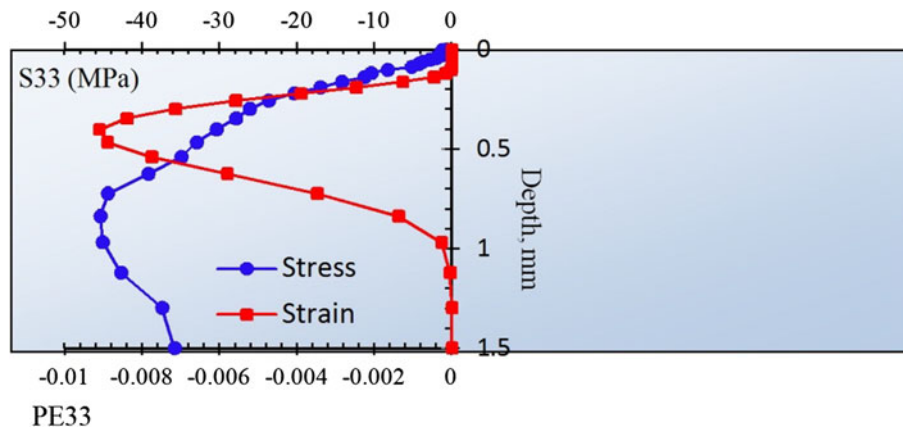


Fig. 13 Max. S33 and PE33 in the subsurface

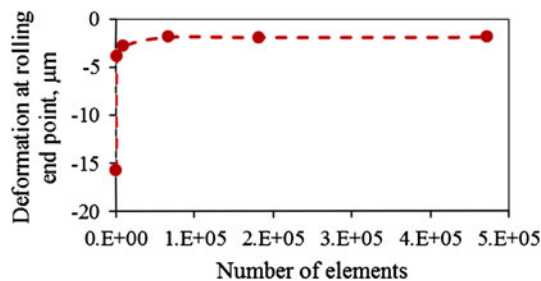


Fig. 14 Deformation at rolling end vs. element number

increases, the deformation value converges. The converged result occurs when the element number is over 67,202.

7. Conclusions

LPB of SE508 Nitinol was performed to study the effect of burnishing pressures on material deformations. A 3D finite element simulation of LPB was also developed to understand burnishing mechanics. The results can be summarized as follows:

- When burnishing pressure increases from 4 to 20 MPa, the depth of burnishing tracks change from 0.2 to 4.0 μm with a percent cold work from 0.01 to 0.2%, respectively.
- A large region of elastic springback of this material could be found when compared to the theoretical deformation amount. The SE property could be observed in this study.
- The predicted and measured profiles of the burnishing tracks are in good agreement. This suggests that the SE-plastic material model can successfully capture the nonlinear behavior of SE508 Nitinol.
- In width direction, S22 stress changes from compression to tension along the path from the tool center, and there exists a neutral point.
- When the applied load changed from 1716.75 to 2540.79 N, the maximum axial compressive residual stress increased from 2.5 to 45.4 MPa. As the load increases, both the depth and magnitude of residual stress

will increase. This compressive residual stress is believed to have a beneficial effect on fatigue life.

- Compressive residual stress 45 MPa occurs at ~ 1.0 mm in subsurface, while compressive residual strain occurs at ~ 0.4 mm. Producing large compressive residual stress in the subsurface with a small amount of shallow deformation is the unique characteristic of LPB process, which can be predicted by the simulation model.

References

1. T. Duerig, A. Pelton, and D. Stockel, An Overview of Nitinol Medical Applications, *Mater. Sci. Eng.*, 1999, **A273–275**, p 149–160
2. A.R. Pelton, S.M. Russell, and J. DiCello, The Physical Metallurgy of Nitinol for Medical Application, *J. Mater.*, 2003, **55(5)**, p 33–37
3. M. Bram, A. SAhmad-Khanlou, A. Heckmann, B. Fuchs, H.P. Buckremer, and D. Stover, Power Metallurgical Fabrication Process for NiTi Shape Memory Alloy Parts, *Mater. Sci. Eng.*, 2002, **A337**, p 254–263
4. V. Imbeni, C. Martini, D. Prandstraller, G. Poli, C. Trepanier, and T.W. Duerig, Preliminary Study of Micro-Scale Wear Behavior of a NiTi Shape Memory Alloy, *J. Wear*, 2003, **254**, p 1299–1306
5. M. Es-Souni and H. Fischer-Brandies, On the Properties of Two Binary NiTi Shape Memory Alloys. Effect of Surface Finish on the Corrosion Behavior and In Vitro Biocompatibility, *Biomaterials*, 2002, **23**, p 2887–2894
6. R. Liu and D.Y. Li, Modification of Archard's Equation by Taking Account of Elastic/Pseudoelastic Properties of Materials, *J. Wear*, 2001, **251**, p 955–964
7. A.R. Pelton, V. Schroeder, M.R. Mitchell, Gong. Xian-Yan, M. Barbet, and S.W. Robertson, Fatigue and Durability of Nitinol Stents, *J. Mech. Behav. Biomed. Mater.*, 2008, **1**, p 153–164
8. FDA, Guidance document for intravascular stents, 2010
9. M.M. EL-Khabeery and M.H. EL-Axir, Experimental Techniques for Studying the Effects of Milling Roller-Burnishing Parameters on Surface Integrity, *Int. J. Mach. Tools Manuf.*, 2001, **41**, p 1705–1719
10. C.Y. Semmikeri, P.K. Brajmankar, and S.B. Mahagaonkar, Investigation of Surface Integrity of AISI, Using LPB Tool, *Tribol. Int.*, 1045, **41(2008)**, p 724–734
11. P.S. Prevey and J.T. Cammett, The Influence of Surface Enhancement by LPB on the Corrosion Fatigue Performance of AA7075-T6, *Int. J. Fatigue*, 2004, **26**, p 975–982
12. P.S. Prevey, R.A. Ravindranath, M. Shepard, and T. Gabb, Case Studied of Fatigue Life Improvement Using LPB in Gas Turbine Engine Applications, *J. Eng. Gas Turbines Power*, 2006, **128**, p 865–872
13. P.S. Prevey, N. Jayaraman, R.A. Ravindranath, and M. Shepard, Mitigation of Fretting Fatigue Damage in Blade and Disk Pressure

- Faces with LPB, *J. Eng. Gas Turbine Power*, 2010, **132**, p 082105-1–082105-8
14. Y.B. Guo and M.E. Barkey, FE-Simulation of the Effects of Machining-Induced Residual Stress Profile on Rolling Contact of Hard Machined Components, *Int. J. Mech. Sci.*, 2003, **46**, p 371–388
 15. M. Šraml, J. Flašker, and I. Potrč, Numerical Procedure for Predicting the Rolling Contact Fatigue Crack Initiation, *Int. J. Fatigue*, 2002, **25**, p 585–595
 16. M. Geetha, A.K. Singh, R. Asokamani, and A.K. Gogia, Ti Based Biomaterials, The Ultimate Choice for Orthopedic Implants—A Review, *Prog. Mater. Sci.*, 2008, **54**, p 397–425
 17. N.B. Morgan, Medical Shape Memory Alloy Applications—The Markets and its Products, *Mater. Sci. Eng.*, 2004, **378**, p 16–23
 18. C.Y. Seemikeri, P.K. Brahmanekar, and S.B. Mahagaonkar, LPB: An Innovative Manufacturing Method for Biomedical Applications, *J. Manuf. Sci. Eng.*, 2008, **130**, p 021008-1–021008-8
 19. J.A. Greenwood, K.L. Johnson, and E. Matsubara, A Surface Roughness Parameter in Hertz Contact, *J. Wear*, 1984, **100**, p 47–57
 20. K.L. Johnson, *Contact Mechanics*, Cambridge University Press, London, 1987, ISBN 0521347963
 21. W. Yan, Q. Sun, X.-Q. Feng, and L. Qian, Analysis of Spherical Indentation of Superelastic Shape Memory Alloys, *Int. J. Solids Struct.*, 2007, **44**, p 1–17
 22. O. Bartier, X. Hernot, and G. Mauvoisin, Theoretical and Experimental Analysis of Contact Radius for Spherical Indentation, *Mech. Mater.*, 2010, **42**, p 640–656
 23. B. Taljat and G.M. Pharr, Development of Pile-up During Spherical Indentation of Elastic-Plastic Solid, *Int. J. Solids Struct.*, 2004, **41**, p 3891–3904
 24. F. Aurichio, M. Panahandeh, and A. Masud, A Finite-Strain Finite Element Model for the Pseudoelastic Behavior of Shape Memory Alloys, *Comput. Meth. Appl. Mech. Eng.*, 1997, **148**, p 23–37
 25. V. Brizmer, Y. Kligerman, and I. Etsion, The Effect of Contact Condition and Material Properties on Elasticity Terminus of a Spherical Contact, *Int. J. Solids Struct.*, 2006, **43**, p 5736–5749
 26. M.G. Knight, L.A. Lacerda, L.C. Wrobel, and J.L. Henshall, Parametric Study of the Contact: Stress Around Spherical and Cylindrical Inclusions, *Comput. Mater. Sci.*, 2002, **25**, p 115–121
 27. X. Hernot, O. Bartier, Y. Bekouche, R. El-Abdi, and G. Mauvoisin, Influence of Penetration Depth and Mechanical Properties on Contact Radius Determination for Spherical Indentation, *Int. J. Solids Struct.*, 2006, **43**, p 4136–4153
 28. W. Yan, Q. Sun, and H.-Y. Liu, Spherical Indentation Hardness of Shape Memory Alloys, *Mater. Sci. Eng.*, 2006, **425**, p 278–285
 29. SIMULIA, *ABAQUS User's Manual*, ver. 6.10, 2010